Navier-Stokes Computations of Transonic Flows with a Two-Equation Turbulence Model

Jubaraj Sahu*
Ballistic Research Laboratory, U.S. Army LABCOM, Aberdeen Proving Ground, Maryland
and
James E. Danberg†
University of Delaware, Newark, Delaware

A thin-layer Navier-Stokes code has been used to compute the turbulent flow over two axisymmetric bodies at transonic speeds. A critical element of calculating such flows is the turbulence model. Numerical computations have been made with an algebraic eddy viscosity model and the $k-\epsilon$ two-equation model. The $k-\epsilon$ equations are developed in a general spatial coordinate system and incorporated into the thin-layer, compressible, time-dependent Navier-Stokes code. The same implicit algorithm that simultaneously solves the Reynolds-averaged mean flow equations is extended to solve the turbulence field equations using block tridiagonal matrix inversions. Calculations with the $k-\epsilon$ model are extended up to the wall. Numerical solutions have been obtained for two transonic flow situations to determine the accuracy of the $k-\epsilon$ model. First, the attached flow over an axisymmetric projectile has been investigated. The second flow situation considered is the transonic separated flow over an axisymmetric bump model. Furthermore, the accuracy and applicability of the $k-\epsilon$ model are determined by comparing the computed results with experimental data.

I. Introduction

THE critical aerodynamic behavior of projectiles occurs in the transonic speed regime. This can be attributed to the complex shock structure that exists on projectiles at transonic speeds. The flowfield is characterized by strong viscous-inviscid shock/boundary-layer interactions and a large separated flow region behind the projectile base. It is advantageous to use the Navier-Stokes computational technique since it considers these interactions in a fully coupled manner.

As part of a continuing research effort at the Ballistic Research Laboratory (BRL), numerical computational capabilities have been developed to predict the aerodynamic behavior of artillery shells. Reference 1 reported the development and application of the azimuthal-invariant, thin-layer, Navier-Stokes computational technique to predict the flow about slender bodies of revolution at transonic speeds. This technique was further extended[2] for complete numerical simulation of a projectile, including the base region. It solves the compressible, thin-layer Navier-Stokes equations in strong conservation form. The equation formulation allows for arbitrary body geometries and is solved using an implicit, approximately factored, finite difference scheme by Beam and Warming.[3] This technique has been used in the present computations.

An important element in calculating flows such as those described above is the turbulence modeling. The simplest model is the algebraic eddy viscosity model. However, it contains a large amount of empiricism that may not, in general, be valid for complex flows.[4,5] Another class includes the two-equation model, which has been popular because it employs less empiricism and allows the flow history to be taken into account. This model has wider applicability to a class of complex fluid flow problems than the algebraic model.[6] The performance of various turbulence models for shock-wave/boundary-layer interaction flows have been made by Coakley and Viegas,[7,8] Viegas and Horstmann,[9] and Marvin.[10] Using a two-equation model in a thin-layer Navier-Stokes code would thus be an important advance and may offer improved prediction especially for flows containing large separation regions. Implicit algorithms that simultaneously solve the mean flow equations can be extended to solve the turbulence field equations using block tridiagonal matrix inversions. The objective of this paper was to incorporate into a thin-layer, time-dependent Navier-Stokes code, a two-equation turbulence model that uses the same implicit algorithm and generalized geometry.

II. Computational Technique

The azimuthal invariant (or generalized axisymmetric) thin-layer Navier-Stokes equations for general spatial coordinates ξ, η, ζ can be written

$$\partial_\tau \boldsymbol{q} + \partial_\xi \boldsymbol{E} + \partial_\zeta \boldsymbol{G} + \boldsymbol{H} = Re^{-1}\partial_\zeta \boldsymbol{S} \tag{1}$$

In Eq. (1) the thin-layer approximation is used and restrictions for axisymmetric flow are imposed. The vector $\boldsymbol{q}$ contains all the dependent variables, i.e., $\boldsymbol{q} = (\rho, \rho u, \rho v, \rho w, e)^T$. The transformed flux vectors $\boldsymbol{E}$ and $\boldsymbol{G}$ are linear combinations of the Cartesian flux vectors, e.g., $\boldsymbol{E} = (\xi_x E + \xi_z G)/J$, where J is the Jacobian of transformation. The source term $\boldsymbol{H}$ results from assuming invariance in the azimuthal direction while viscous terms are contained in the vector $\boldsymbol{S}$. For the computation of turbulent flows, the viscosity μ and the thermal conductivity κ contain their molecular and turbulent parts. The turbulent contribution μ_t and κ_t are supplied through an eddy viscosity hypothesis (a simple algebraic eddy viscosity model and a two-equation $k-\epsilon$ model) described in the following section. In dimensionless form, $\mu = \kappa$ for constant Prandtl number.

Presented as Paper 85-0373 at the AIAA 23rd Aerospace Sciences Meeting, Reno, NV, Jan. 14-17, 1985; received June 5, 1985; revision received Feb. 13, 1986.

*Aerospace Engineer, Launch and Flight Division. Member AIAA.
†Professor, Department of Mechanical and Aerospace Engineering. Associate Fellow AIAA.

The numerical algorithm used is the Beam-Warming, fully implicit, approximately factored finite difference scheme. The algorithm can be first- or second-order accurate in time and second- or fourth-order accurate in space. Since the interest is only in the steady-state solution, Eq. (1) is solved in a time-asymptotic fashion, and first-order-accurate time differencing is used. The spatial accuracy is fourth-order. Details of the algorithm are described in Refs. 3, 11, and 12.

III. Turbulence Models

Algebraic Eddy Viscosity Model

The algebraic eddy viscosity model used is the one developed by Baldwin and Lomax.[13] It is a two-layer model in which an eddy viscosity is calculated for an inner and an outer region. The inner region follows the Prandtl-Van Driest formulation. In both the inner and outer formulations, the distribution of vorticity is used to determine the length scales, thereby avoiding the necessity of finding the outer edge of the boundary layer. For the inner region,

$$(\mu_T)_{\text{inner}} = \rho \ell^2 |\omega| \tag{2}$$

where

$$\ell = \kappa y[1 - \exp(-y^+/A^+)]$$

$$y^+ = (\rho_w u_\tau y)/\mu_w \qquad u_\tau = \sqrt{(\tau_w/\rho_w)}$$

and $|\omega|$ is the absolute magnitude of vorticity. The eddy viscosity for the outer region is given by

$$(\mu_T)_{\text{outer}} = KC_{\text{cp}} \rho F_{\text{wake}} F_{\text{kleb}}(y) \tag{3}$$

where $F_{\text{wake}} = y_{\max} F_{\max}$ or $C_{\text{wk}} y_{\max} u_{\text{dif}}^2 / F_{\max}$, the smaller of the two values. The quantities $y_{\max}$ and $F_{\max}$ are determined from the function $F(y) = y|\omega|[1 - \exp(-y^+/A^+)]$, where $F_{\max}$ is the maximum value of $F(y)$ and $y_{\max}$ is the value of y at which it occurs. The function $F_{\text{kleb}}(y)$ is the Klebanoff intermittency factor. The quantity u_{dif} is the difference between the maximum and minimum total velocity in the profile and, for boundary layers, the minimum is defined as zero.

The outer formulation can be used in wakes as well as in attached and separated boundary layers. For free-shear flow regions or wakes, the Van Driest damping term $[\exp(-y^+/A^+)]$ is neglected. It is necessary to specify the following constants; $A^+ = 26$, $C_{\text{cp}} = 1.6$, $C_{\text{kleb}} = 0.3$, $C_{\text{wk}} = 0.25$, $\kappa = 0.4$, and $K = 0.0168$. This type of simple model is generally inadequate for complex flows. One model that has been used successfully to predict many flows and has wider applicability is the two-equation $k - \epsilon$ model.

Two-Equation $k - \epsilon$ Model

The two-equation model used here is Chien's[14] $k - \epsilon$ model, which is similar to that of Jones and Launder.[15] To be consistent with the mean flow equations, the turbulent kinetic energy (k) and dissipation rate (ϵ) equations have been transformed to a body-fitted coordinate system.

Governing Equations

The transformed $k - \epsilon$ equations can be written in a form similar to Eq. (1),

$$\frac{\partial \boldsymbol{q}_t}{\partial \tau} + \frac{\partial \boldsymbol{E}_t}{\partial \xi} + \frac{\partial \boldsymbol{G}_t}{\partial \zeta} = \frac{1}{Re}\left(\frac{\partial \boldsymbol{H}_t}{\partial \zeta} + \boldsymbol{S}_t\right) \tag{4}$$

where

$$\boldsymbol{q}_t = \frac{1}{J}\begin{bmatrix} \rho k \\ \rho \epsilon \end{bmatrix} \qquad \boldsymbol{E}_t = \frac{1}{J}\begin{bmatrix} \rho k U \\ \rho \epsilon U \end{bmatrix} \qquad \boldsymbol{G}_t = \frac{1}{J}\begin{bmatrix} \rho k W \\ \rho \epsilon W \end{bmatrix}$$

$$\boldsymbol{H}_t = \frac{1}{J}\begin{bmatrix} \left(\zeta_x^2 + \zeta_y^2 + \zeta_z^2\right)\left(\frac{\mu_t}{\sigma_k} + \mu\right)\frac{\partial k}{\partial \zeta} \\ \left(\zeta_x^2 + \zeta_y^2 + \zeta_z^2\right)\left(\frac{\mu_t}{\sigma_\epsilon} + \mu\right)\frac{\partial \epsilon}{\partial \zeta} \end{bmatrix}$$

$$\boldsymbol{S}_t = \frac{1}{J}\begin{bmatrix} P - \rho\epsilon Re - 2\mu\frac{k}{y_n^2} \\ c_1\frac{\epsilon}{k}P - C_2\rho\frac{\epsilon^2}{k}Re - 2\mu\frac{\epsilon}{y_n^2}\exp^{-y^+/2} \end{bmatrix}$$

and P is the production term given as

$$P = \mu_t\left(\zeta_x^2 + \zeta_y^2 + \zeta_z^2\right)\left(u_\zeta^2 + v_\zeta^2 + w_\zeta^2\right) + \mu_t\left(\zeta_x u_\zeta + \zeta_y v_\zeta + \zeta_z w_\zeta\right)^2$$

This constitutes a low Reynolds number formulation of the $k - \epsilon$ model. Calculations are extended up to the wall itself, and exact values of the dependent variables at the wall are used as boundary conditions. Chien's model is better behaved mathematically near a solid wall and is thus utilized in this study.

The $k - \epsilon$ model employs the eddy viscosity concept and relates eddy viscosity to the turbulent kinetic energy and dissipation rate as

$$\mu_t = c_\mu \rho\left(k^2/\epsilon\right) \tag{5}$$

The empirical coefficients in Eqs. (4) and (5) must be specified:

$$c_1 = 1.44$$

$$c_2 = 1.92\left[1 - 0.3\exp\left(-R_t^2\right)\right]$$

$$c_3 = 2.0, \qquad \sigma_k = 1.0, \qquad \sigma_\epsilon = 1.3$$

$$c_\mu = 0.09[1 - \exp(-0.01 y^+)]$$

where $R_t = k^2/\nu\epsilon$.

Solution Algorithm

The turbulence field equations described above are solved using the same implicit scheme and approximate factorization used for the mean flow equations. A convenient solution algorithm is developed for Eq. (4) with the following sequence:

$$\left[(I - \Delta t D^n) + \Delta t\left(\delta_\zeta B^n - \delta_\zeta C^n\right)\right]\Delta\tilde{q}^n = \text{RHS}\,(4) \tag{6a}$$

$$\left[I + \Delta t\,\delta_\xi A^n\right]\Delta q^n = \Delta\tilde{q}^n \tag{6b}$$

$$q^{n+1} = q^n + \Delta q^n \tag{6c}$$

where RHS (4) is the right-hand side of Eq. (4). First, Eq. (6a) is solved for $\Delta\tilde{q}^n$ since the right-hand side is known at the old time step. $\Delta\tilde{q}^n$ becomes the right-hand side of Eq. (6b), which is then solved for $\Delta\tilde{q}^n$. This is then added to q^n to give q^{n+1} at the next time step, as shown in Eq. (6c). A, B, and C are the Jacobian matrices resulting from the local linearization of the flux terms $\boldsymbol{E}_t$, $\boldsymbol{G}_t$, and $\boldsymbol{H}_t$. Near the wall, the source terms $\boldsymbol{S}_t$ (production, dissipation, diffusion, and decay) become dominant over the convection term and can be very large. This can result in a very stiff algorithm if the source terms are treated entirely in an explicit manner. Thus, they are treated implicitly and form the Jacobian matrice D, which is included in the ζ operator for convenience.

The Jacobian matrices are given as

$$A = \begin{bmatrix} U & 0 \\ 0 & U \end{bmatrix} \qquad B = \begin{bmatrix} W & 0 \\ 0 & W \end{bmatrix}$$

$$C = \begin{bmatrix} \alpha_k \frac{\partial}{\partial \zeta}\left(\frac{J}{\rho}\right) & 0 \\ 0 & \alpha_\epsilon \frac{\partial}{\partial \zeta}\left(\frac{J}{\rho}\right) \end{bmatrix}$$

$$D = \begin{bmatrix} \left(2C_\mu \frac{k}{\epsilon} P - Re^{-1} \frac{2\mu}{\rho y_n^2}\right)\left(-C_\mu \frac{\kappa^2}{\epsilon^2} P - 1\right) \\ \left(c_1 C_\mu P + c_2 \frac{\epsilon^2}{k^2}\right)\left(-2c_2 \frac{\epsilon}{k} - Re^{-1} \frac{2\mu}{\rho y_n^2} \exp^{-y^+/2}\right) \end{bmatrix}$$

where

$$\alpha = \frac{Re^{-1}}{J}\left(\frac{\mu_t}{\sigma} + \mu\right)\left(\zeta_x^2 + \zeta_y^2 + \zeta_z^2\right)$$

The operators δ_ξ and δ_ζ are central difference operators. Usually fourth-order dissipation terms are added explicitly to control numerical instability. For the turbulence field variables, convective terms often dominate the diffusion in the far field (away from the wall) and can cause convective instability. To overcome this difficulty, numerical smoothing based on an upwind scheme[16] is used. The details of the algorithm and the method of solution for the turbulent variables can be found in Ref. 17.

Initial and Boundary Conditions

Convection terms are negligible near the wall. The largest terms over a large portion of the boundary layer are the production and dissipation. Based on local equilibrium, the production term can be equated to the dissipation term to obtain the initial k and ϵ profiles. The turbulent viscosity μ_t appears in the production term and is obtained from the solution with an algebraic eddy viscosity model. The above assumption works well for attached, wall-bounded flows but may be poor for separated or free-shear flows.

Since calculations are extended up to the wall, it is easier to specify the boundary conditions on the wall. At the wall, the dependent variables are zero, i.e., $k = \epsilon = 0$. In the far field, which lies outside the edge of the boundary layer, zero derivatives of k and ϵ are used. At the upstream boundary, k and ϵ are set to zero. A first-order extrapolation is used at the downstream boundary.

Coupling with Mean Flow Equations

Equation (1) is solved first by the Beam-Warming, fully implicit, approximately factored finite difference scheme for the mean flow quantities. Next, the turbulence field equation (4) is solved using the just computed mean flow quantities. The same implicit finite difference algorithm used to solve the Reynolds-averaged mean flow equations is used to solve the turbulence field equations. For the turbulence variables, this reduces to a 2×2 block tridiagonal system of equations, which are rapidly solved. Solution of Eq. (4) gives k and ϵ, and Eq. (5) is then used to compute μ_t. This then becomes the input in the solution of Eq. (1) for mean flow variables, and this process is continued at each time step until steady-state results are achieved. The solution procedure of the turbulence field equations thus lags that of the mean flow equations by one time step.

IV. Results

Numerical computations have been made for two transonic turbulent flow cases: 1) attached flow over an axisymmetric projectile, and 2) separated flow over an axisymmetric bump model. Comparison with experimental data has been made to assess the performance of both turbulence models.

Attached Flow over an Axisymmetric Projectile

The transonic flowfield about a projectile configuration with a turbulent boundary layer has been computed. All the computed results shown are for $\alpha = 0$ deg, $Re = 13 \times 10^6$/m, and $M = 0.94$ and are compared with experimental measurements.[18] The model geometry is shown in Fig. 1. It is a simplified form of an artillery projectile consisting of a secant-ogive nose, a cylindrical midsection and a 7-deg conical afterbody or boattail of half a caliber (1 caliber ≡ 1 diameter).

The computational grid used for the numerical computations was obtained from a versatile grid-generation program[19] that allows grid point clustering near the body surface. The grid consists of 78 points in the longitudinal direction and 40 points in the normal direction. An expanded view of the grid near the model is shown in Fig. 2. The dark region near the model surface results from clustering of grid points that are needed to resolve the viscous boundary-layer region. The grid points in the normal direction were exponentially stretched away from the surface with a mimimum spacing at the wall of 0.00002 D, which corresponds to a $y^+ \simeq 1$.

The turbulence quantities k and ϵ obtained with the two-equation turbulence model are shown in Figs. 3 and 4, respectively, for selected longitudinal stations. Figure 3 shows the turbulence kinetic energy profiles in the law-of-the-wall coordinate. The station $X/D = 5.05$ is in front of the boattail corner, and $X/D = 5.36$ is just after the boattail corner. Because of the severe expansion at the boattail junction, the turbulence kinetic energy is increased by a factor of 2 between these stations. It then drops off on the boattail as shown by the profiles at stations $X/D = 5.61$ and 6.19. The humps in these profiles are believed to be the result of the interaction of

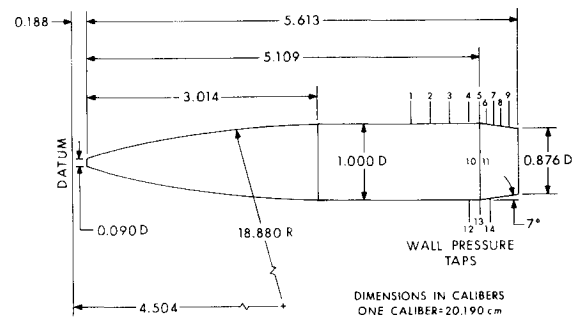

Fig. 1 Model geometry.

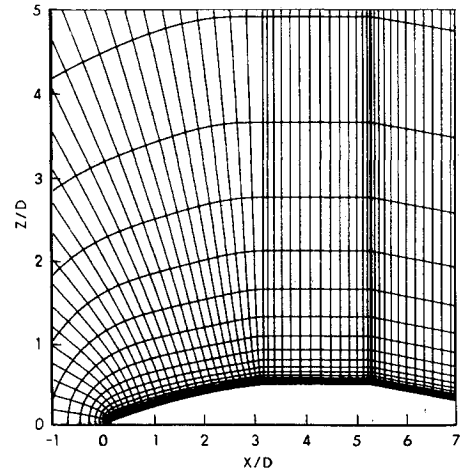

Fig. 2 Expanded view of the grid near the projectile.

the shock and expansion waves with the turbulent boundary layer and occur outside the edge of the boundary layer. The peaks in the k profiles occur at $y^+ \simeq 20$. As shown in Fig. 4, the turbulence dissipation rate profiles show identical behavior for the same stations, with the exception that there are no humps present in the region outside the edge of the boundary layer. Additionally, the peaks now occur closer to the wall, at $y^+ \simeq 10$. This agrees with the observed behavior of the peaks in Ref. 5.

Turbulent eddy viscosities are found from k and ϵ with the two-equation model and the algebraic Baldwin and Lomax model.[13] These are referenced to the molecular viscosity μ_∞ and plotted in Figs. 5 and 6. Figure 5 shows the μ_t profiles obtained with the algebraic model. The profiles have rather flat peaks and go to zero outside the boundary layer. The eddy viscosity, μ_t drops off sharply in magnitude near the boattail corner, i.e., $X/D = 5.05$-5.36 and then rises sharply on the boattail as seen by the profiles between $X/D = 5.61$ and 6.19. The algebraic model is based on local information and results in sharp increases or decreases in μ_t. The μ_t profiles obtained with the $k-\epsilon$ model, on the other hand, show gradual change in μ_t on the boattail as seen in Fig. 6. The profiles have sharper peaks and then fall off to values other than zero outside the edge of the boundary layer. Although k and ϵ profiles drop off to practically zero, k^2/ϵ does not drop off from its peak value monotonically with increasing distance from the surface and results in nonzero μ_t. The mean flow gradients outside the boundary layer are, however, exceedingly small, and these μ_t in no way adversely affect the solution of the mean flow quantities.

Figure 7 shows the mean velocity profiles at the same selected stations. Both models predict almost the same profile at $X/D = 5.05$, and comparison with experiment is good. Just downstream of the boattail corner, i.e., at $X/D = 5.36$ and

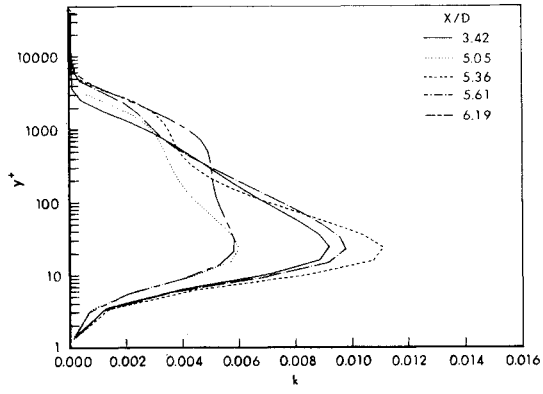

Fig. 3 Turbulent kinetic energy profiles, $M_\infty = 0.94$, $\alpha = 0$.

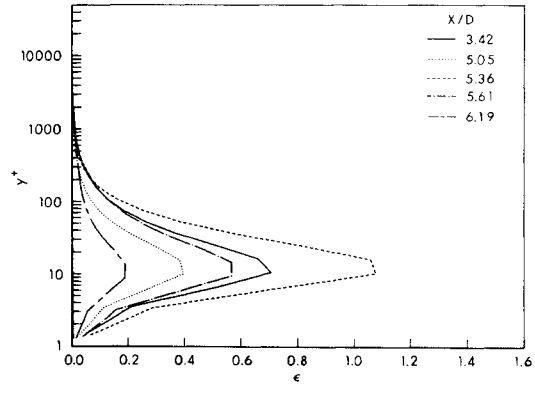

Fig. 4 Turbulent dissipation rate profiles, $M_\infty = 0.94$, $\alpha = 0$.

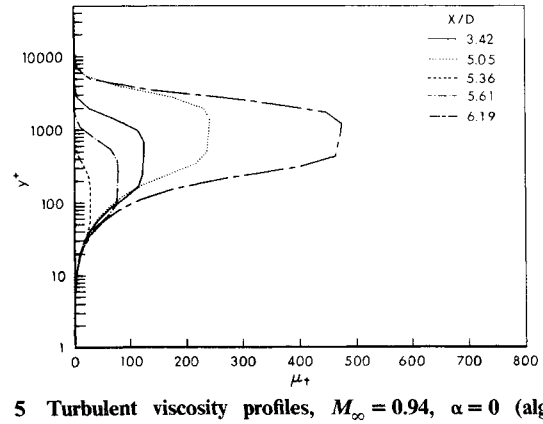

Fig. 5 Turbulent viscosity profiles, $M_\infty = 0.94$, $\alpha = 0$ (algebraic model).

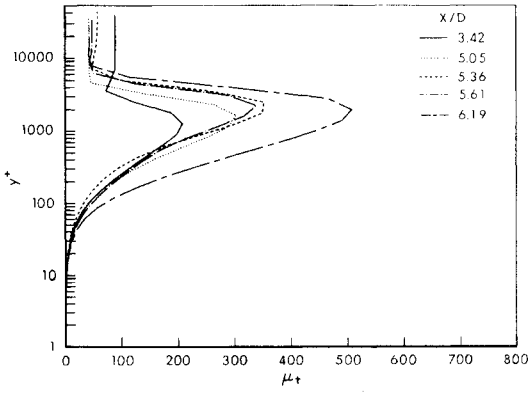

Fig. 6 Turbulent viscosity profiles, $M_\infty = 0.94$, $\alpha = 0$ ($k-\epsilon$ model).

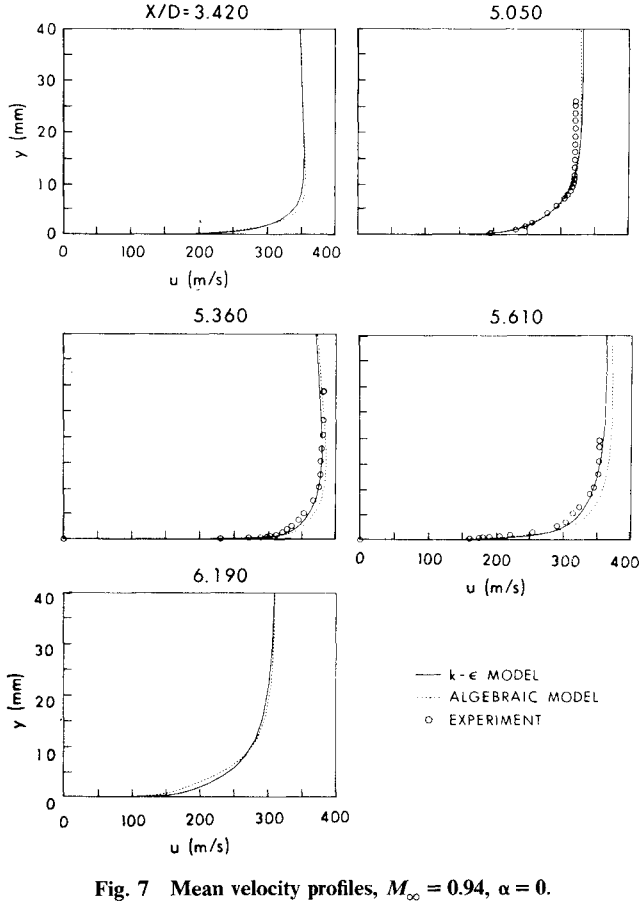

Fig. 7 Mean velocity profiles, $M_\infty = 0.94$, $\alpha = 0$.

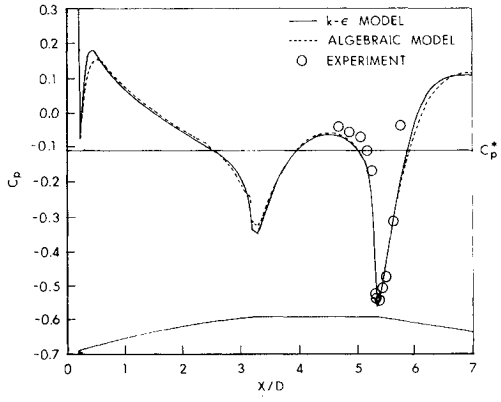

Fig. 8 Surface pressure distribution, $M_\infty = 0.94$, $\alpha = 0$.

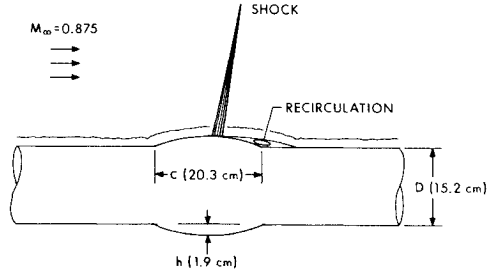

Fig. 9 Schematic illustration of the bump model.

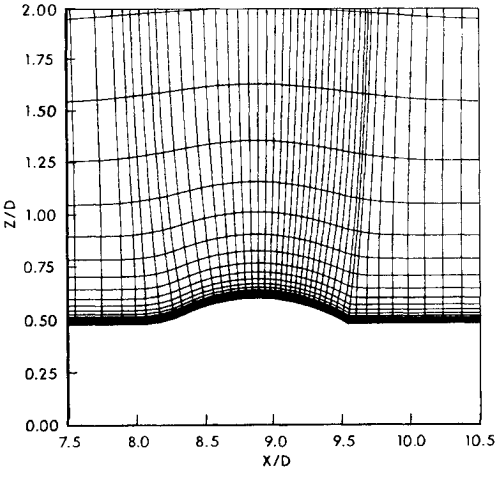

Fig. 10 Expanded grid near the bump.

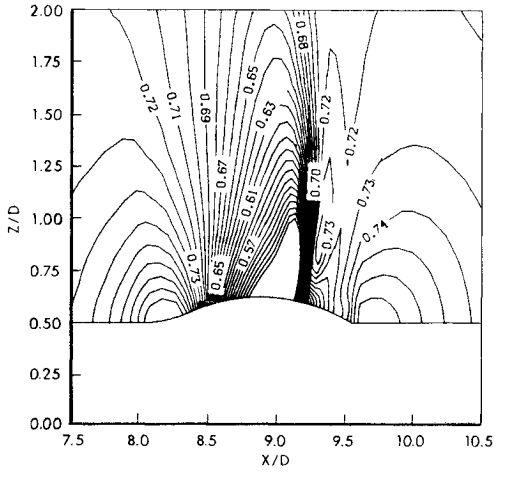

Fig. 11 Pressure contours, $M_\infty = 0.875$, $\alpha = 0$.

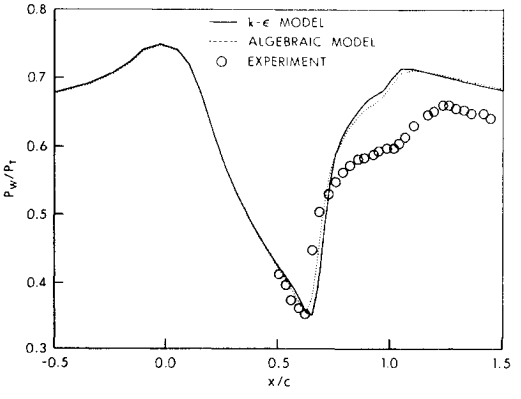

Fig. 12 Surface pressure distribution, $M_\infty = 0.875$, $\alpha = 0$.

5.61, comparison of the $k-\epsilon$ calculations with experiment is in better agreement than the algebraic model predictions are. Figure 8 is a plot of the surface pressure distribution as a function of the longitudinal position over the projectile. Computed results obtained with both models are in good agreement with experiment. A small improvement of the results with the $k-\epsilon$ model can be seen on the boattail.

Separated Flow over an Axisymmetric Bump

Numerical computations have been made for a transonic turbulent separated flow over a bump model. All the computed results shown are for $M = 0.875$, $\alpha = 0$ deg and $Re = 13.6 \times 10^6$/m. Experimental measurements of the mean flow quantities, as well as the turbulence variables for the same model, have been made by Johnson et al.[20] Calculated results using both the algebraic and $k-\epsilon$ models are compared with these experimental data.

A schematic diagram of the model and its associated flowfield are shown in Fig. 9. The model consists of an annular circular-arc bump affixed to a thin-walled cylinder of outer diameter 15.2 cm. The bump has a thickness of 1.9 cm and a chord length of 20.3 cm. Its leading edge is joined to the cylinder by a smooth circular arc of radius 18.3 cm, which is tangent to the cylinder at 3.33 cm upstream and to the bump at 2.05 cm downstream of the intersection of the arc of the bump with the cylinder. In other words, a fairing is used in the leading edge of the bump. The flowfield contains a separated region that is induced by a shock wave.

The computational mesh for this case was obtained using a hyperbolic grid generator, which is an extension of the work reported in Ref. 19. Figure 10 shows an expanded view of the grid near the bump model. Most of the grid points are clustered on the aft portion and just downstream of the circular-arc bump in the flow direction. The grid points in the normal direction were exponentially stretched away from the wall. The first point was taken to be 0.00001 D away from the model surface, which corresponds to y^+ of about 0.5. The number of grid points used was 78 and 40 in the longitudinal and normal direction, respectively.

The upstream boundary conditions were prescribed by uniform freestream conditions. First-order extrapolation was used at the downstream boundary. The no-slip boundary condition was used on the wall, and freestream conditions were used at the far-field outer boundary. For the turbulence variables with the $k-\epsilon$ two-equation model, k and ϵ were set to zero on the wall and at the upstream boundary. Zero derivatives of k and ϵ were used at the outer and downstream boundaries.

Figure 11 shows the pressure contours in the flowfield near the bump. As can be seen, the flow expands over the front portion of the model. The shock wave can be clearly seen to exist on the aft portion of the circular-arc bump. These

qualitative features are predicted by both the algebraic and $k-\epsilon$ models. Figure 12 is a plot of the surface pressure distribution as a function of the longitudinal position. The longitudinal position in this plot and plots to follow is referenced to the leading edge of the bump excluding the fairing, i.e., the intersecting point of the arc of the bump with the cylinder (see Fig. 10). The position of the shock wave is well predicted by both the models; however, there is a small disagreement in the region downstream of the shock. The largest discrepancy is about 15% and could be due partly to the large grid spacings used in the redeveloping flow region and possibly to the level of eddy viscosity in the separation region (at least for the algebraic model). Figure 13 shows the skin-friction coefficient distribution as a function of longitudinal position. It clearly shows the separated flow region for which $c_f < 0$. The $k-\epsilon$ model predicts a thinner reversed flow region compared to the algebraic model. Additionally, the $k-\epsilon$ model predicts a much sharper rise in c_f in the flow redevelopment region compared to the slow rise of c_f predicted by the algebraic model.

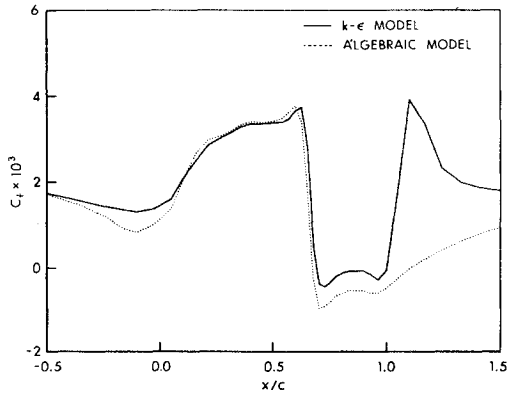

Fig. 13 Skin-friction coefficient, $M_\infty = 0.875$, $\alpha = 0$.

Development of the mean velocity, turbulent shear stress, and turbulent kinetic energy profiles over the aft portion and just downstream of the bump are shown in Figs. 14-16, respectively. The mean velocity profiles are shown in Fig. 14. Flow separation occurs at $x/c = 0.875$. The mean velocity profiles in the separated region are shown through $x/c = 1.062$. As pointed out earlier, the $k-\epsilon$ model predicts a thin reversed flow region. This is especially true at the stations selected in the separated region. Away from the wall, the $k-\epsilon$ model calculations show better agreement with the experimental data. Poor predictions by both models can be observed at $x/c = 1.125$, which is a station just upstream of reattachment. The redevelopment of the flow after reattachment is shown at $x/c = 1.25$ and 1.375, and here the $k-\epsilon$ model produced a solution that more closely represents the experimental data than did the algebraic model.

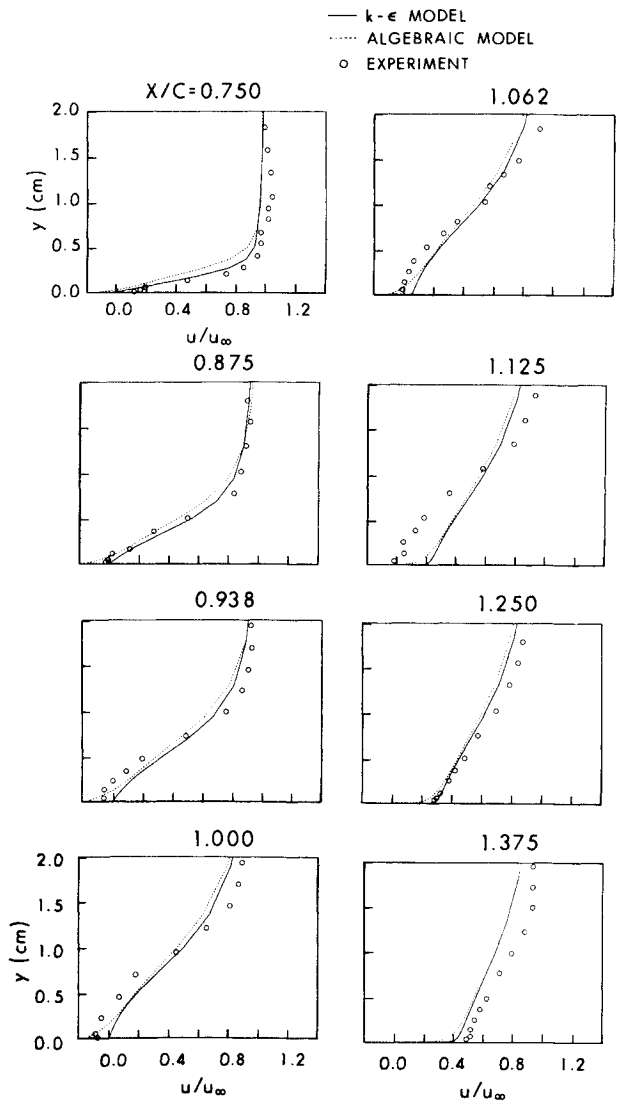

Fig. 14 Mean velocity profiles, $M_\infty = 0.875$, $\alpha = 0$.

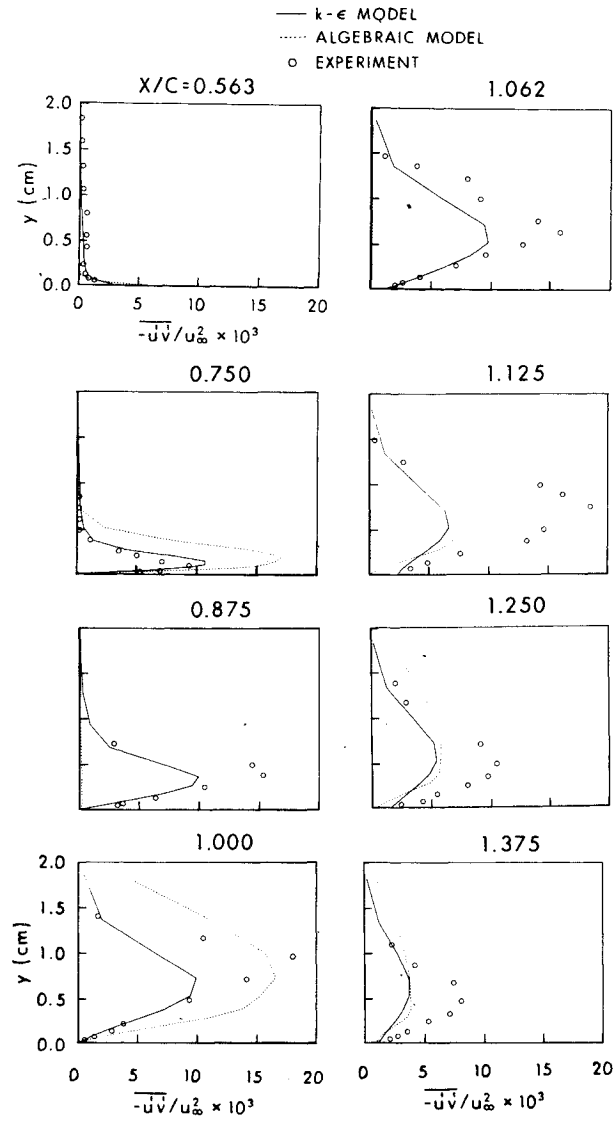

Fig. 15 Turbulent shear stress profiles, $M_\infty = 0.875$, $\alpha = 0$.

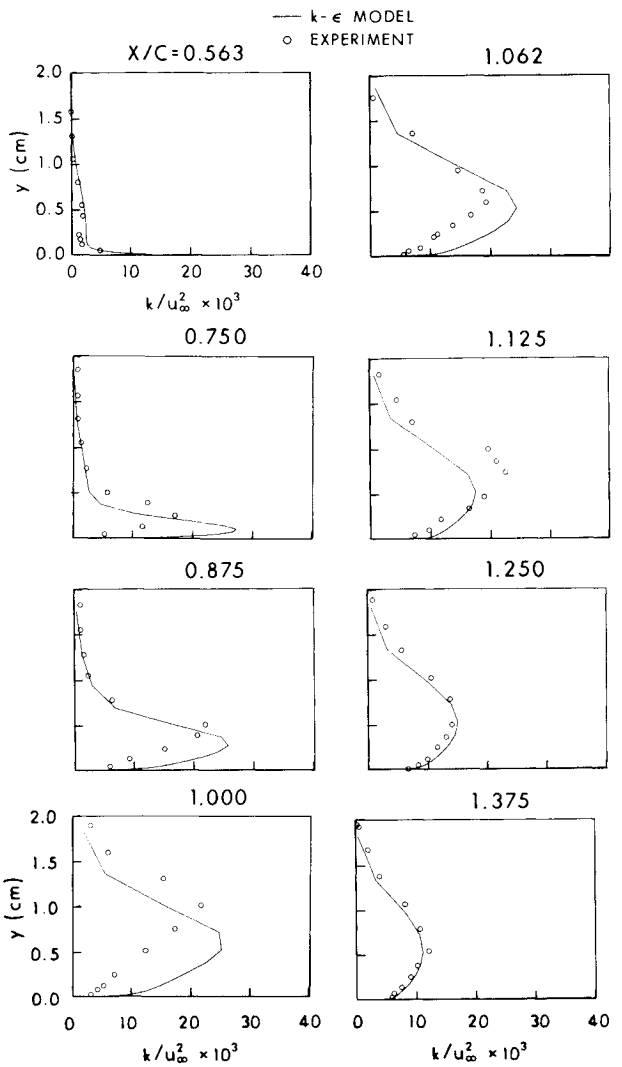

Fig. 16 Turbulent kinetic energy profiles, $M_\infty = 0.875$, $\alpha = 0$.

Figure 15 shows the turbulent shear stress at selected streamwise stations. As evident from this figure, the $k-\epsilon$ model predicts the turbulent shear stress profiles which are in close qualitative agreement with the experimental data. The peaks are not as well predicted however. Additionally, the location of the peaks shifts further away from the wall just as determined experimentally, and the $k-\epsilon$ model successfully predicts the rate of peak displacement for $x/c = 0.563$-1.062. The algebraic model, on the other hand, predicts sharp increase or decrease in the turbulent shear stress as seen for $x/c = 0.75$ thru 1.125. It grossly underpredicts the turbulent shear stress at $x/c = 0.875$ and 1.062.

The turbulent kinetic energy profiles at the same selected stations are shown in Fig. 16. The profile at a station upstream of the shock ($x/c = 0.563$) compares well with experimental measurements. The profiles in the separated region are shown for $x/c = 0.75$-1.125. The magnitude of the peaks are well predicted by the two-equation $k-\epsilon$ model although the location of the peaks are slightly offset. Comparison of the profiles very close to the wall indicate poor predictions. In the redeveloping flow region after reattachment, the computed profiles with the $k-\epsilon$ model are in excellent agreement with the experimental data. This is where we have seen good agreement in the mean velocity profiles as well. The location of the maximum turbulent shear stress is shown in Fig. 17. The locations are well predicted by the $k-\epsilon$ model and are in close agreement with the experimental observations except near $x/c = 1$, i.e., where the aft end of the bump is affixed to the cylinder.

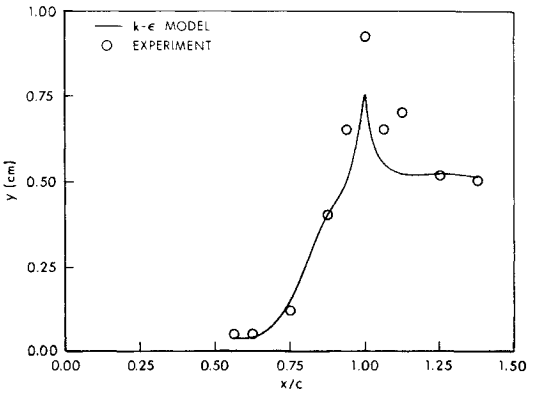

Fig. 17 Location of maximum turbulent shear stress, $M_\infty = 0.875$, $\alpha = 0$.

All the computations were performed on a VAX 780 computer. Each solution was marched in time until a steady result was obtained. A typical transonic flow calculation with an algebraic turbulence model took about 1400 time steps to converge, whereas the same calculation with a $k-\epsilon$ turbulence model took 1800 time steps. Computation with algebraic model ran at a speed of 0.0115 s/time step/point. As expected, the corresponding speed with the $k-\epsilon$ model was larger, 0.0126 s/time step/point. This resulted in about 40% additional CPU time with the $k-\epsilon$ turbulence model. The same time steps were used for both models, and the stability of the code was not affected.

V. Concluding Remarks

The $k-\epsilon$ turbulence model was formulated in a general spatial coordinate system and incorporated into a compressible, thin-layer Navier-Stokes code. The same implicit algorithm used to solve the Navier-Stokes equations was extended to solve the turbulence field equations for the $k-\epsilon$ model. Numerical computations were made of two transonic turbulent flow cases: 1) attached flow over a projectile at $M_\infty = 0.94$ and 2) separated flow over an axisymmetric bump model at $M_\infty = 0.875$. Computations for these cases were also made using an algebraic eddy viscosity model. Computed results obtained by both turbulence models were compared with experimental data.

The algebraic model is based on local information and predicts sharp increases and decreases in turbulent shear stress, which may be unrealistic. The $k-\epsilon$ model predicts gradual change in turbulence quantities. Computed results show generally good agreement with experimental data except in the separated region. Some improvements in the flow redevelopment region were found with the $k-\epsilon$ model. Future work will be directed toward improving the prediction in the separated flow region and the application of the $k-\epsilon$ turbulence model in the wake or base flow behind the projectile.

References

[1] Nietubicz, C.J., Pulliam, T.H., and Steger, J.L., "Numerical Solution of the Azimuthal-Invariant Thin-Layer Navier-Stokes Equations," *AIAA Journal*, Vol. 18, Dec. 1980, pp. 1411-1412.

[2] Sahu, J., Nietubicz, C.J., and Steger, J.L., "Navier-Stokes Computations of Projectile Base Flow with and without Base Injection," *AIAA Journal*, Vol. 23, Sept. 1985, pp. 1348-1355.

[3] Beam, R. and Warming, R.F., "An Implicit Factored Scheme for the Compressible Navier-Stokes Equations," AIAA Paper 77-645, June 1977.

[4] Gorski, J.J., Govindan, T.R., and Lakshminarayana, B., "Computation of Three-Dimensional Turbulent Shear Flows in Corners," AIAA Paper 83-1733, July 1983.

[5] Van Gulick, P., "Application of the Turbulence Model to a Turbulent Boundary Layer Solutions for Flow about a Spinning Yawed Projectile at Mach 3," Master's Thesis, University of Delaware, Newark, DE, June 1983.

[6]Launder, B.E. and Spalding, D.B., *Mathematical Models of Turbulence*, Academic Press, Orlando, FL, 1972.

[7]Coakley, T.J. and Viegas, J.R., "Turbulence Modeling of Shock Separated Boundary-Layer Flows," Paper presented at the Symposium on Turbulent Shear Flows, University Park, PA, April 1977.

[8]Viegas, J.R. and Coakley, T.J., "Numerical Investigation of Turbulence Models for Shock-Separated Boundary-Layer Flows," *AIAA Journal*, Vol. 16, April 1978, pp. 293-294.

[9]Viegas, J.R. and Horstman, C.C., "Comparison of Multi-Equation Turbulence Models for Several Shock Boundary-Layer Interaction Flows," *AIAA Journal*, Vol. 17, Aug. 1979, pp. 811-820.

[10]Marvin, J.G., "Turbulence Modeling for Computational Aerodynamics," AIAA Paper 82-0164, Jan. 1982.

[11]Steger, J.L., "Implicit Finite Difference Simulation of Flow about Arbitrary Geometries with Application to Airfoils," *AIAA Journal*, Vol. 16, July 1978, pp. 679-686.

[12]Pulliam, T.H. and Steger, J.L., "On Implicit Finite-Difference Simulations of Three-Dimensional Flow," *AIAA Journal*, Vol. 18, Feb. 1980, pp. 159-167.

[13]Baldwin, B.S. and Lomax, H., "Thin Layer Approximation and Algebraic Model for Separated Turbulent Flows," AIAA Paper 78-257, Jan. 1978.

[14]Chien, K.-Y., "Predictions of Channel and Boundary-Layer Flows with a Low-Reynolds-Number Turbulence Model," *AIAA Journal*, Vol. 20, Jan. 1982, pp. 33-38.

[15]Jones, W.P. and Launder, B.E., "The Prediction of Laminarization with a Two-Equation Model of Turbulence," *International Journal of Heat and Mass Transfer*, Vol. 15, 1972.

[16]Chakravarthy, S.R. and Osher, S., "Numerical Experiments with the Osher Upwind Scheme for the Euler Equations," AIAA Paper 82-0975, June 1982.

[17]Sahu, J., "Navier-Stokes Computational Study of Axisymmetric Transonic Turbulent Flows with a Two-Equation Model of Turbulence," Ph.D. Dissertation, University of Delaware, Newark, DE, June 1984.

[18]Nietubicz, C.J., Inger, G.R., and Danberg, J.E., "A Theoretical and Experimental Investigation of a Transonic Projectile Flow Field," AIAA Paper 82-0101, Jan. 1982.

[19]Steger, J.L., Nietubicz, C.J., and Heavey, K.R., "A General Curvilinear Grid Generation Program for Projectile Configurations," U.S. Army Ballistic Research Laboratory, Aberdeen Proving Ground, MD, ARBRL-MR03142, Oct. 1981.

[20]Johnson, D.A., Horstman, C.C., and Bachalo, W.D., "Comparison Between Experiment and Prediction for a Transonic Turbulent Separated Flow," *AIAA Journal*, Vol. 20, June 1982, pp. 737-744.